



### Key Points:

- Individually, common roughness metrics (rugosity and standard deviation) do not quantify horizontal scales of variability, limiting utility
- For multiscale natural topography, it is important to consider elevation distribution moments, length scale ratios, and power law scaling
- A principal component analysis illustrates how multiple metrics covary and identifies dominant modes of topographic variability

### Correspondence to:

J. L. Hench,  
jim.hench@duke.edu

### Citation:

Duvall, M. S., Hench, J. L., & Rosman, J. H. (2019). Collapsing complexity: Quantifying multiscale properties of reef topography. *Journal of Geophysical Research: Oceans*, 124, 5021–5038. <https://doi.org/10.1029/2018JC014859>

Received 13 DEC 2018

Accepted 18 MAY 2019

Accepted article online 7 JUN 2019

Published online 22 JUL 2019

## Collapsing Complexity: Quantifying Multiscale Properties of Reef Topography

Melissa S. Duvall<sup>1</sup> , James L. Hench<sup>1</sup> , and Johanna H. Rosman<sup>2</sup> 

<sup>1</sup>Marine Laboratory, Nicholas School the Environment, Duke University, Beaufort, NC, USA, <sup>2</sup>Institute of Marine Sciences, University of North Carolina at Chapel Hill, Morehead City, NC, USA

**Abstract** Seafloor topography affects a wide range of physical and biological processes; therefore, collapsing the three-dimensional structure of the bottom to roughness metrics is a common challenge in studies of marine systems. Here we assessed the properties captured by metrics previously proposed for the seafloor, as well as metrics developed to characterize other types of rough surfaces. We considered three classes of metrics: properties of the bottom elevation distribution (e.g., standard deviation), length scale ratios (e.g., rugosity), and metrics that describe how topography varies with spatial scale (e.g., Hölder exponents). The metrics were assessed using idealized topography and natural seafloor topography data from airborne lidar measurements of a coral reef. We illustrate that common roughness metrics (e.g., rugosity) can have the same value for topographies that are geometrically very different, limiting their utility. Application of the wavelet leaders technique to the reef data set demonstrates that the topography has a power law scaling behavior, but it is multifractal so a distribution of Hölder exponents is needed to describe its scaling behavior. Using principal component analysis, we identify three dominant modes of topographic variability, or ways metrics covary, among and within reef zones. Collectively, the results presented here show that coral reef topography is both multiscale and multifractal. While individual metrics that capture specific topography properties relevant to a given process may be suitable for some studies, many applications will require a set of metrics that includes statistics that capture how topography varies with spatial scale.

### 1. Introduction

The structural complexity of benthic topography has important effects on ecological processes and hydrodynamics in coastal and marine systems. The physical structure of the substrate determines habitat availability (Harbome et al., 2012; Sale et al., 1984), species abundance and biodiversity (Friedlander & Parrish, 1998), and surface area for material fluxes (e.g., Falter et al., 2004). Benthic topography also has a first-order effect on hydrodynamics by imposing forces (Asher et al., 2016) on moving water and increasing momentum and scalar dispersion (Jones et al., 2008). In turn, this can influence rates of nutrient uptake (Atkinson & Bilger, 1992), photosynthesis (Dennison & Barnes, 1988; Patterson et al., 1991), and calcification (Comeau et al., 2014; Dennison & Barnes, 1988) of benthic organisms. Despite its importance, quantifying the physical structure of bottom topography remains a challenge, as reef topography is often patchy and discontinuous and varies over orders of magnitude in spatial scale, from millimeters to kilometers.

A variety of statistical metrics have been used to quantify topography, and these metrics capture and describe different properties of a curve or surface. Previous studies have utilized metrics that describe bottom structure in terms of roughness, which is defined as the departure from a flat geometric profile or surface (Hearn, 2011). Two common roughness metrics are standard deviation and rugosity. Standard deviation ( $\sigma$ ) is a second-moment order description of the distribution of surface elevation and is a measure of the total amount of vertical variability in the topography. Rugosity ( $R$ ) is a ratio of the contour length along the surface of the substrate to the corresponding projected horizontal length and is a measure of how much vertical variation increases the path length of substrate relative to a flat line. Ecological studies on reefs have primarily used rugosity as a measure of bottom roughness (Dahl, 1973; Luckhurst & Luckhurst, 1978; McCormick, 1994; Risk, 1972), and previous hydrodynamic studies have used standard deviation (Lowe et al., 2005) and root mean square (rms) slope (Rogers et al., 2018), which is closely related to rugosity.

While these metrics can be useful, they do not alone uniquely define or differentiate surfaces. For example, consider an idealized one-dimensional topography represented by  $b(x) = A \cos(kx)$ , where  $b(x)$  is bottom

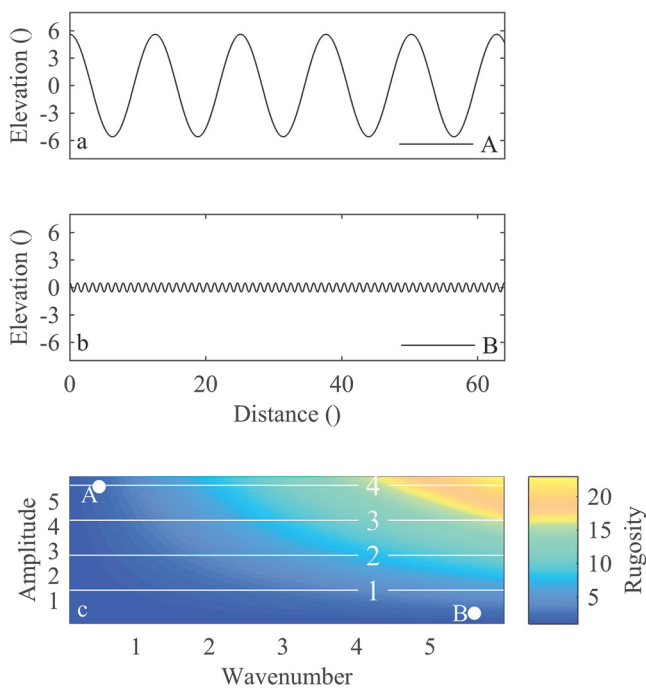


**Figure 1.** Comparison of idealized one-dimensional topographies derived from cosine functions. The high-amplitude and low-wave number topography (a) has the same rugosity value as the low-amplitude and high-wave number topography (b). Permutations of different amplitudes and wave numbers (c) yield the same rugosity (colors) and standard deviation of topography (white lines).

fractional Brownian motion) for which a single Hurst exponent defines the change in topographic variation with scale everywhere along the spatial series or surface (Lavallée et al., 1993; Muzy et al., 1994).

Monofractal methods cannot be used to determine the presence or absence of multiple scaling behaviors within a signal (Gagnon et al., 2006). It has been shown that multifractality is ubiquitous across many geographical and geophysical systems (Lavallée et al., 1993; Lovejoy & Schertzer, 1990; Tchiguirinskaia et al., 2000; Weissel et al., 1994; Wendt et al., 2009), meaning that different spatial locations can exhibit different scaling behaviors, and therefore the change in topographic variation with scale is defined by a statistical distribution of exponents rather than a single exponent. These local exponents, known as Hölder exponents ( $h$ ), are found using the power law scaling behavior of a range of moment orders of elevation increments along a topographic transect. For natural topography, the scaling behavior and fractal dimension derived from each of these approaches depends on the choice of method and scale range considered.

Although monofractal and multifractal methods account for topographic variability across multiple scales, like standard deviation and rugosity, individual parameters derived from these methods (e.g., Hölder exponent) are also incomplete descriptors of roughness for multiscale topography. It has been shown in terrestrial systems that topographic surfaces with the same scaling behavior can possess different variances of surface elevation (Weissel et al., 1994). Thus, scaling exponents alone may not capture differences between dissimilar surfaces. This underscores the need for a conceptual framework to better understand the properties of the topography captured by different roughness metrics.

Roughness metrics may be classified as (1) metrics that describe the distribution of bottom elevation, (2) metrics that describe ratios of physical length scales, and (3) metrics that describe topographic variation with spatial scale. Metrics that describe the elevation distribution, such as the statistical moment orders, describe the probability density function of the spatial series without regard to the sequence or ordering of

elevation,  $A$  is amplitude, and  $k$  is wave number. Standard deviation,  $\sigma(A, k)$ , and rugosity,  $R(A, k)$  can be computed analytically for  $b(x)$  for any combination of amplitude and wave number. Low wave number, high-amplitude topographic spatial series can have the same rugosity as high-wave number, low-amplitude series (Figure 1). For this example the standard deviation only depends on the amplitude of the spatial series, while rugosity depends on both amplitude and wave number (Figure 1c). Thus, both standard deviation and rugosity can yield the same values for geometrically dissimilar topographies, raising questions about whether additional parameters could improve characterizations of bottom roughness in ecological and hydrodynamic studies on reefs.

Commonly applied roughness metrics that describe the distribution of elevation (e.g., standard deviation) or ratios of physical length scales (e.g., rugosity and root mean square (rms) bottom slope), do not describe topographic variation with spatial scale for multiscale topography. Recognizing the need for this third type of roughness metric, previous studies have examined the power law relationship between a given measure of topographic variability and horizontal spatial scale. Methods that have been applied to bottom topography include the variation method, which quantifies the scaling behavior from variations in elevation extremes as a function of spatial scale (Zawada et al., 2010; Zawada & Brock, 2009), and the box counting method, based on the number of boxes of progressively smaller sizes needed to cover a curve or surface (Martin-Garin et al., 2007; Purkis et al., 2005; Purkis et al., 2007). Other approaches include the change in spectral density (Jaramillo & Pawlak, 2011; Nunes & Pawlak, 2008) or rugosity (Knudby & LeDrew, 2007) across a range of spatial scales. A limitation of the aforementioned techniques is that only a single global scaling exponent, known as the Hurst exponent, can be computed for a given curve or surface. These methods are only appropriate for monofractal mathematical processes (e.g., fractional Brownian motion) for which a single Hurst exponent defines the change in topographic variation with scale everywhere along the spatial series or surface (Lavallée et al., 1993; Muzy et al., 1994).

the data. On the other hand, metrics that describe ratios of physical length scales, such as the rugosity, aspect ratio, or slope, describe topographic variation by relating vertical and horizontal length scales that are determined by the ordering of elevation data along the series or surface. The third category of metrics associates topographic variation with each horizontal length scale in order to determine the dominant scales of variability or the change in topographic variability across a range of scales.

Metrics chosen to quantify the properties of topography should have a physical interpretation, permit reliable comparisons between topography at multiple sites or at a single site over time, and be relevant to ecological and hydrodynamic applications. The aim of this study is to analyze the statistical properties of coral reef topography and assess the extent to which important topography properties are captured by different metrics. Metrics from the three aforementioned categories are applied to spatial series from idealized synthetic surfaces as well as natural coral reef bathymetry. We evaluate the capacity for different metrics to discern geometrically dissimilar topography occurring across and within zones of a coral reef, as well as how they capture different topographic properties. We also examine how different metrics covary with each other and the implications for determining what descriptors are needed to adequately describe multiscale reef topography.

## 2. Methods

Here we define the methods used to compute the following metrics from each of the three aforementioned categories: (1) mean, standard deviation, skewness, and kurtosis; (2) rugosity; and (3) Hurst and Hölder exponents. We then describe two data sets, topography measurements from a coral reef, and idealized fractional Brownian motion (fBm) spatial series with known geometric properties that we use as a reference for comparison.

### 2.1. Metrics That Describe the Distribution of Elevation

We computed the first four statistical moments of the distribution of bottom elevation. Mean ( $\bar{b}$ ), standard deviation ( $\sigma$ ), skewness ( $S$ ), and kurtosis ( $K$ ) were computed directly from spatial series of bottom elevation,  $b(x_i)$ :

$$\bar{b} = \frac{1}{N} \sum_{i=1}^N b(x_i), \quad (1)$$

$$\sigma = \sqrt{\frac{1}{N} \sum_{i=1}^N |b(x_i) - \bar{b}|^2}, \quad (2)$$

$$S = \frac{\frac{1}{N} \sum_{i=1}^N [b(x_i) - \bar{b}]^3}{\left( \sqrt{\frac{1}{N} [b(x_i) - \bar{b}]^2} \right)^3}, \quad (3)$$

$$K = \frac{\frac{1}{N} \sum_{i=1}^N [b(x_i) - \bar{b}]^4}{\left( \frac{1}{N} \sum_{i=1}^N [b(x_i) - \bar{b}]^2 \right)^2}, \quad (4)$$

where  $N$  is the number of elevation points in the series.

### 2.2. Metrics That Describe a Ratio of Physical Length Scales

We computed the rugosity (i.e., ratio of length along the surface of the substrate to corresponding projected horizontal length) of each spatial series using the expression:

$$R = \frac{\sum_{i=1}^{N-1} \sqrt{\Delta b_i^2 + \Delta x^2}}{(N-1)\Delta x} = \frac{1}{(N-1)} \sum_{i=1}^{N-1} \sqrt{1 + \left(\frac{\Delta b_i}{\Delta x}\right)^2}, \quad (5)$$

where  $\Delta x = x_{i+1} - x_i$  is the horizontal resolution of the spatial series, assumed here to be uniform and  $\Delta b_i = b(x_{i+1}) - b(x_i)$  is the local bathymetric gradient. A related set of metrics have been proposed that quantify frontal area per unit plan area or concentration of roughness elements area, such as the rms bottom slope (e.g., Rogers et al., 2018; Wooding et al., 1973)

$$\left(\frac{db}{dx}\right)_{rms} = \sqrt{\frac{1}{N-1} \sum_{i=1}^{N-1} \left(\frac{\Delta b_i}{\Delta x}\right)^2}. \quad (6)$$

Note that  $R$  and  $(db/dx)_{rms}$  are both functions of the local bottom slope and hence are closely related. We therefore considered only rugosity in our analyses.

### 2.3. Metrics That Describe Topographic Variation With Scale

#### 2.3.1. Monofractal Metrics

To quantify the global scaling behavior, we computed the power spectral density, which has been previously used in the coral reef literature to quantify how topography varies as a function of spatial scale (Jaramillo & Pawlak, 2011; Nunes & Pawlak, 2008). The power spectrum was computed following Welch's (1967) method

$$P(k) = \frac{1}{nNU} \sum_{i=0}^{N-1} \left| \sum_{m=0}^{n-1} w_m b_{m+iv} e^{-2\pi kmj} \right|^2, \quad (7)$$

where  $N$  is the number of segments for which the Fourier transform is computed,  $n$  is the number of points in a given segment,  $w$  is a window function (Hann used here),  $j = \sqrt{-1}$ , and  $v$  is the number of points a successive segment is offset; for example, for a 50% window overlap  $v = n/2$ .  $U$  is given by

$$U = \frac{1}{n} \sum_{m=0}^{n-1} |w_m|^2. \quad (8)$$

Linear trends were removed prior to computing  $P(k)$ .

The Hurst exponent,  $H$  (Hurst, 1951), was computed from the spectral density, a second-moment order descriptor of the global scaling behavior (Gagnon et al., 2006; Seuront, 2010). The spectral density,  $P$ , decays with wave number,  $k$ , according to the power law

$$P = Ak^{-\beta}. \quad (9)$$

The scaling exponent  $\beta$  was computed from a linear fit to the power spectrum over the spatial scale range  $4 \leq 1/k \leq 256$  (fBm: unitless; natural bathymetry: meters) as the relationship between  $P$  and  $k$  was approximately linear over this range (Meakin, 1998). For fBm series,  $\beta$  computed from a spectral density function is related to  $H$  by the expression  $H = \frac{1}{2}(\beta - 1)$ . For the natural reef bathymetry,  $\beta$  was computed over the same wave number range using the same approach. However, it is known that the estimator of Hurst exponents from the slope of the power spectrum is biased if a signal is multifractal because of small shifts in the spectral density due to the resolution dependence of the multifractal process (Gagnon et al., 2006). We therefore applied a correction, derived from our multifractal analyses, to our Hurst exponent estimates for the natural bathymetry. The corrected Hurst exponent was computed as  $H = (\beta - \tau(2))/2$  where similar to  $\beta$ ,  $\tau(2)$  is a second-moment order description of the change in topographic variability as a function of spatial scale (see section 2.3.2 below; Gagnon et al., 2006; Lovejoy et al., 2008; Watson et al., 2009; Yu et al., 2011).

#### 2.3.2. Multifractal Metrics

We calculated the distribution of Hölder exponents ( $h$ ) that define the local scaling behavior of the signal, using a multifractal wavelet leaders technique. Wavelets act as “generalized oscillating boxes” that preserve the self-similarity of nonstationary series; therefore, they are effective tools for examining scaling behavior (Arneodo et al., 2002; Daubechies, 1990; Mallat, 2009; Torrence & Compo, 1998). We chose the

wavelet leaders technique because it allows for a complete characterization of the distribution of Hölder exponents within the spatial series (i.e., both positive and negative moment orders are numerically stable; Muzy et al., 1993; Wendt et al., 2009).

The power law scaling behavior is determined from the partition functions,  $Z(s, q)$ , which are computed as spatial averages of the wavelet leaders,  $l_x$ , at a given scale  $s$  and  $q$ th order.

$$Z(s, q) = \frac{1}{n_s} \sum_{x=1}^{n_s} |l_x(s, x)|^q, \quad (10)$$

where  $l_x(s, x)$  are the wavelet leaders defined as the largest wavelet coefficients obtained from the discrete wavelet transform within a narrow spatial neighborhood,  $x$ , at any finer scale  $s' \leq s$ , and  $n_s$  is the number of wavelet leaders at a given scale (Wendt et al., 2007, 2009). To compute  $Z(s, q)$ , an orthonormal Daubechies wavelet with two vanishing moments ( $N_\psi = 2$ ) was applied at scales  $4 \leq s \leq 32$  m (scales larger than 32 m were not included due to boundary effects) and moment orders  $-2 \leq q \leq 2$ . The relationship between the partition function,  $Z(s, q)$ , and spatial scale,  $s$ , is expressed in terms of a power law with scaling exponent  $\tau(q)$  defined as (Wendt et al., 2009)

$$Z(s, q) \sim As^{\tau(q)}, \quad (11)$$

where  $A$  is a constant. The exponent  $\tau(q)$  was calculated as the slope of the relationship between the logarithm of  $Z(s, q)$  and the logarithm of  $s$ . To compute the multifractal spectrum,  $D(h)$ , where  $D$  is the Hausdorff dimension that describes the amount of space explained by a set of points associated with a given  $h$  value (Wendt et al., 2009), we used a Legendre transform for the set of all  $q$  values that are real numbers, which gives the greatest upper bound for  $D(h)$  ensuring the spectrum is concave

$$D(h) = \inf_{q \in \mathbb{R}} [d + qh - \tau(q)], \quad (12)$$

where  $d$  is the dimension of the data (e.g.,  $d = 1$  for transects) and  $h = d\tau/dq$ . Although wavelet-based multifractal analysis can be built directly on the wavelet coefficients, using the wavelet leaders gives more accurate multifractal spectra for both monofractal (e.g., fBm) and multifractal (e.g., multiplicative cascades) processes (Jaffard et al., 2006; Lashermes et al., 2008).

The multifractal spectrum,  $D(h)$ , can be described by the  $h$  value at which  $D(h)$  is a maximum, together with the width and asymmetry of the distribution  $D(h)$ . These parameters correspond to the first, second, and third log cumulants  $c_p$  ( $c_1$ ,  $c_2$ , and  $c_3$ ) of the polynomial expansion of the multifractal spectrum (Wendt et al., 2009)

$$D(h) = d + \frac{c_2}{2!} \left( \frac{h-c_1}{c_2} \right)^2 + \frac{-c_3}{3!} \left( \frac{h-c_1}{c_2} \right)^3 + \frac{-c_4 + 3c_3^2/c_2}{4!} \left( \frac{h-c_1}{c_2} \right)^4 + \dots \quad (13)$$

The estimation of the log cumulants did not significantly change when a wavelet function with a larger number of vanishing moments ( $N_\psi$ ) was used (cf. Wendt et al., 2009). We also found that the symmetry of the wavelet basis function (e.g., right asymmetry, left asymmetry, and symmetric) had little influence on the resulting multifractal spectrum. For a detailed introduction to the wavelet leaders approach and an implementation in MATLAB, we refer the reader to Wendt et al. (2009).

## 2.4. Data

### 2.4.1. Idealized Reef Topography: Fractional Brownian Motion

Fractional Brownian motion (fBm) is an example of a monofractal process that has been used as a model for reef bathymetry (Purkis & Kohler, 2008), as well as other natural topography (Goodchild, 1980; Mandelbrot, 1975). While fBm does not capture nonlinear or spatially varying scaling behaviors that often occur in natural topography, it is used here to demonstrate the difference between monofractal and multifractal processes. An fBm series,  $B_H(x)$ , is a Gaussian process whose increments have a

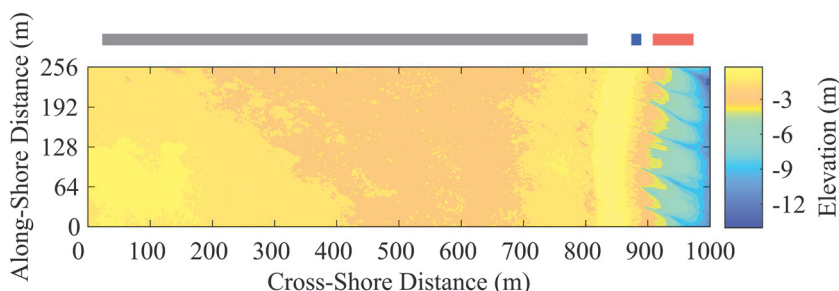


**Figure 2.** Lidar bottom elevation data for natural reef study site on the southeast side of Moorea, French Polynesia. Along-shore transects 256 m in length were extracted every meter from a 256-m by 1,000-m swath. Horizontal colored lines indicate spatial extent of backreef (gray), reef crest (blue), and fore reef (red) transects included in analysis.

covariance function that is described by a single prescribed Hurst exponent  $H$  (Mandelbrot & van Ness, 1968). When  $0 < H < 0.5$ , the increments of  $B_H$  are negatively correlated, qualitatively representing rougher topography. When  $0.5 < H < 1$ , the increments of  $B_H$  are positively correlated, representing smoother topography. When  $H = 0.5$ , the increments of  $B_H$  are independent or uncorrelated, representing ordinary Brownian motion (Mandelbrot & van Ness, 1968). Herein, we used the wavelet-based synthesis of fBm described in Abry and Sellan (1996).

All fBm spatial series were 256 data points in length and were generated for  $H$  values between 0 and 1. Global ( $H$ ) and local ( $h$ ) scaling exponents were then estimated empirically from each spatial series using the methods described in sections 2.3.1 and 2.3.2 and were compared with the known theoretical value of  $H$  used to generate the spatial series. The fBm model was used as a monofractal example with known scaling to verify the accuracy of each method for estimating  $H$  from spatial series, the appropriateness of user-defined parameters (e.g., wavelet choice and scale range), and the uncertainties associated with applying the methods to relatively short spatial series. This was necessary before computing scaling exponents using the same methods for spatial series from natural reef topography with unknown scaling.

#### 2.4.2. Natural Reef Topography

Metrics were computed for spatial series extracted from bathymetric data for a natural reef surrounding Moorea, French Polynesia. The bathymetric data were collected in June 2015 using a high-resolution airborne topohydrographic lidar system (RIEGL VQ-820-G) with a data acquisition rate of 251 kHz. For this survey, horizontal accuracy was 1 m and vertical accuracy was 0.23 m for depths less than 5 m at a 95% confidence level (Fugro LADS Corporation, 2015). A 1-m gridded bathymetric data product was generated by computing the mean of bottom elevation values measured within 1-m by 1-m squares. From this data set, 1,000 alongshore transects, each 256 m in length, were extracted from a 256-m by 1,000-m swath on the southeast side of Moorea. The swath included the backreef, reef crest, and shallow fore reef zones (Figure 2). The length of the alongshore transects was limited to 256 m due to the lack of well-formed spur and groove features over long distances, the curved reef crest, and a desire for all transects to be oriented approximately parallel to shore. We chose not to compute two-dimensional spatial metrics of the entire swath because one of the main objectives of this study was to compare roughness metrics among the three reef zones. The morphology of the reef (e.g., the narrow reef crest zone), as well as data constraints (e.g., lidar bathymetry data were limited to depths shallower than ~12 m), prohibited us from extracting swaths of sufficient size from each reef zone to perform analysis in two dimensions.

The three areas of the reef consist of geometrically dissimilar coral formations. The backreef topography is comprised of coral aggregations less than one to several meters in size that are separated by areas of sand, rubble, and reef pavement (Leichter et al., 2013). The reef crest topography consists of relatively flat pavement and coral rubble that is intersected by narrow channels running perpendicular to the shoreline. The fore reef is characterized by low-wave number spur and groove formations running approximately perpendicular to the reef crest from 2- to  $\geq 60$ -m depth (Leichter et al., 2013). Roughness metrics were computed for 781 backreef, 17 reef crests, and 69 fore reef transects, as some of the alongshore transects were omitted from analysis due to insufficient data coverage.

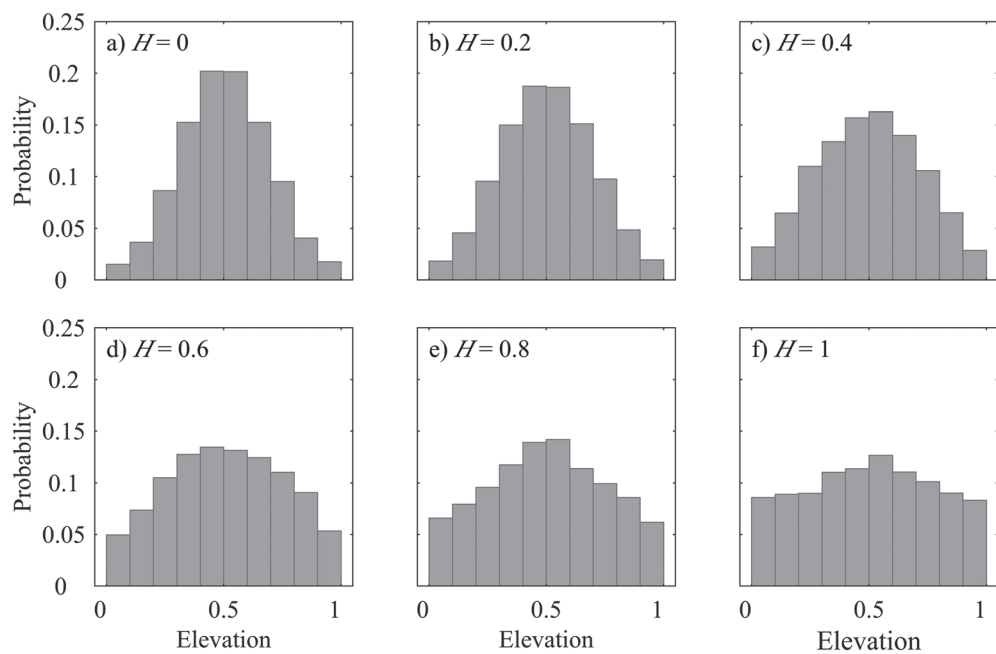


**Figure 3.** Histograms displaying the average fraction of observations within a given elevation interval for 100 fBm transects defined by a given  $H$  value.

### 3. Results

#### 3.1. Moments of the Distribution of Elevation

Histograms of elevation were computed for fBm transects defined by various values of  $H$  (Figure 3). The values for each transect were normalized to vary between 0 and 1 while still preserving the scaling behavior. Because fBm is a Gaussian process, it has a normal, bell-shaped distribution that can be completely described by its second-order statistics. As  $H$  increases, the mean remains roughly the same while the

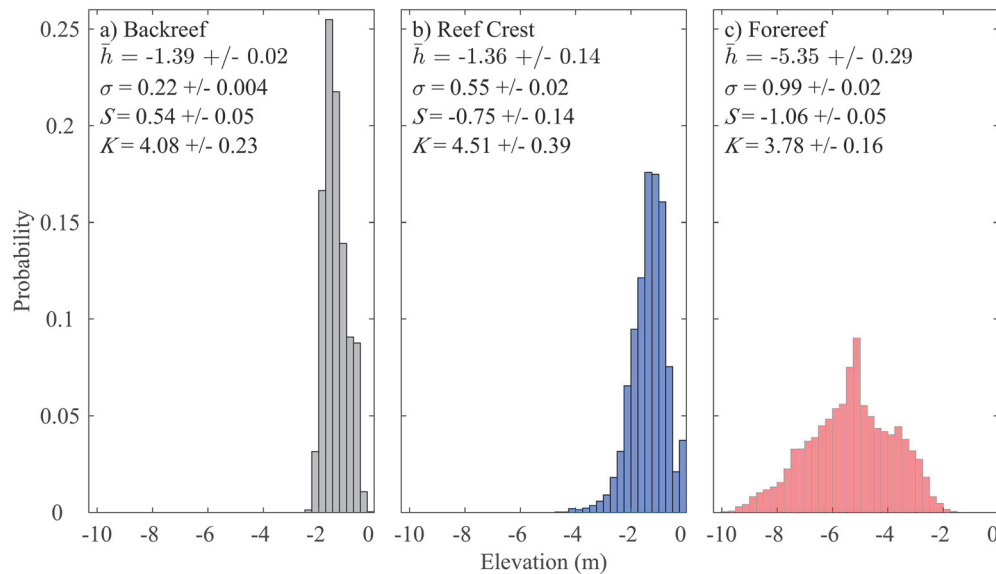


**Figure 4.** Histograms displaying the average fraction of observations within a given elevation interval for all along-shore transects within the backreef, reef crest, or forereef zone. The first four moment orders of the distribution of elevation values were computed for all transects. For each reef zone, the mean and  $2 \times$  standard error are reported for each moment order.

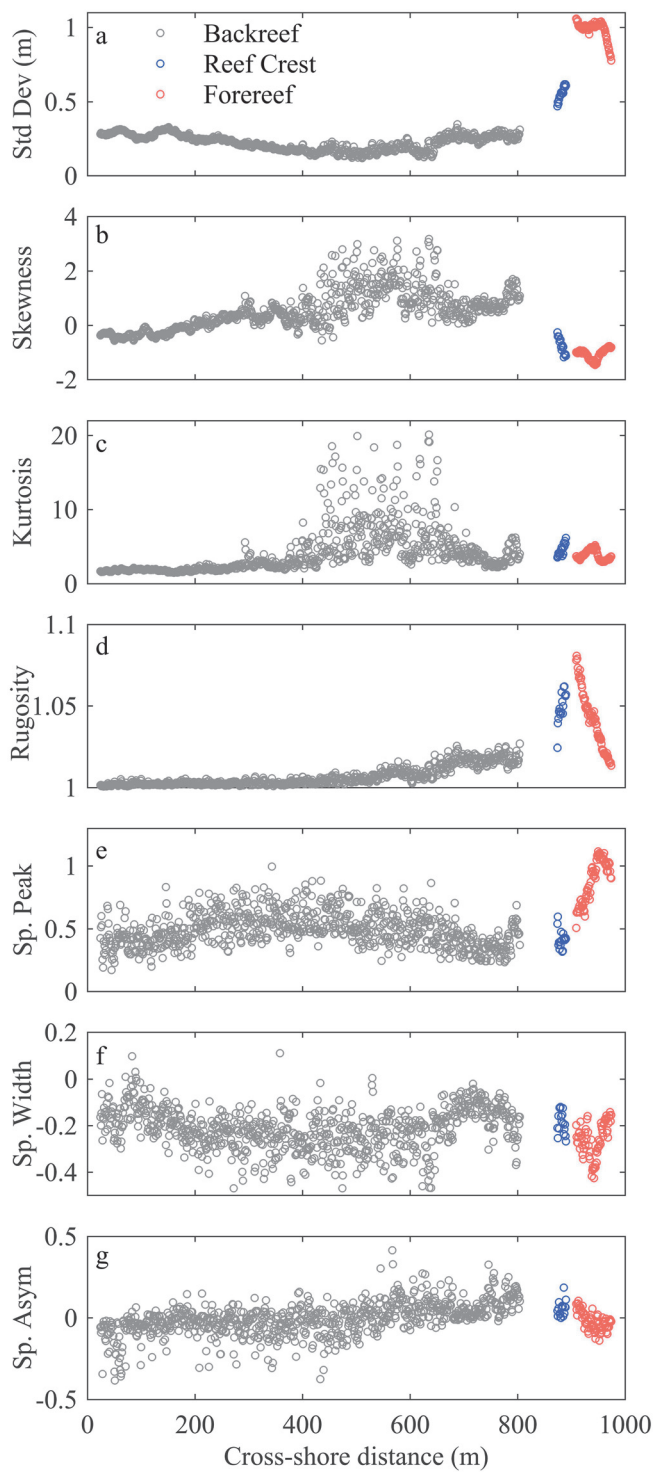


**Figure 5.** (a) Standard deviation (m), (b) skewness, (c) kurtosis, (d) rugosity, (e) spectral peak, (f) spectral width, and (g) spectral asymmetry of  $D(h)$  as a function of cross-shore distance for the backreef, reef crest, and forereef areas of the reef.

from shore, while standard deviation remains near constant. This pattern could indicate little change in the amplitude of large spur and groove features that dominate the standard deviation but a decrease in the size of smaller-scale variations in topography that affect rugosity.

standard deviation increases. For low  $H$  values, the fact that displacements from adjacent elevation points are negatively correlated constrains the fBm series from drifting far away from the mean, thereby also constraining the standard deviation and creating a qualitatively rough spatial series. For high  $H$  values, consecutive displacements are correlated, allowing a fBm series to diverge from the mean, resulting in a high standard deviation driven by large, smooth undulations in the series.

For the natural reef topography, statistical moments of the distributions of elevation were computed for backreef, reef crest, and forereef bathymetric transects. Mean distributions were computed for each reef zone (Figure 4), and the second, third, and fourth moment orders are shown as a function of cross-shore distance (Figures 5a–5c). The mean elevation is similar for the backreef and reef crest ( $\bar{b}_{br} = -1.39$  m;  $\bar{b}_{rc} = -1.36$  m), where the water depths are similar, and much more negative for the forereef ( $\bar{b}_{fr} = -5.35$  m; Figure 4). Standard deviation, which quantifies the size of vertical variations in the topography, increases with distance from shore, such that it is the lowest in the backreef ( $\sigma_{br} = 0.22$  m), intermediate on the reef crest driven by narrow channels intersecting the reefscape ( $\sigma_{rc} = 0.55$  m), and highest on the forereef due to the presence of high-amplitude spur and groove features ( $\sigma_{fr} = 0.99$  m; Figures 4 and 5a). Unlike fBm, higher-order statistical moments (e.g., skewness and kurtosis) are needed to describe the distributions of natural bathymetry. Mean skewness decreases with distance from shore, such that the backreef bathymetry exhibits positive skewness (i.e., skewed to the right;  $S_{br} = 0.54$ ) corresponding to a relatively flat reef substrate with superimposed coral bommies that deviate positively away from the mean (Figures 4 and 5b). Generally, the bathymetry in the reef crest and forereef zones exhibits negative skewness ( $S_{rc} = -0.75$  and  $S_{fr} = -1.06$ ) due to the presence of small channels intersecting the relatively flat rubble bathymetry on the reef crest and large grooves on the forereef adjacent to spur features. Kurtosis does not follow a cross-shore trend, as the highest mean kurtosis is on the reef crest ( $K_{rc} = 4.51$ ), lowest on the forereef ( $K_{fr} = 3.78$ ), and intermediate in the backreef ( $K_{br} = 4.08$ ; Figures 4 and 5c). Higher kurtosis on the reef crest reflects infrequent yet relatively large deviations away from the flat bathymetry due to narrow, deep channels. Lower kurtosis on the forereef reflects frequent, relatively modest-sized deviations consistent with the low-wave number, sinusoidal spur and grooves. Only standard deviation and skewness are significantly different for the three reef zones at the 95% confidence level ( $p < 0.05$ ).

### 3.2. Rugosity

Rugosity was computed for each backreef, reef crest, and forereef bathymetric transect, (Figure 5d). Generally, the lowest rugosity was found in the nearshore backreef ( $R = 1$  indicates a flat seafloor with no slope or roughness), while the highest rugosity was found on the forereef zone adjacent to the reef crest. On the forereef, the decrease in rugosity with distance from shore can be partially attributed to a decrease in the amplitude of spur and groove features on the outer forereef, which also causes the standard deviation to decrease with distance from shore (Figure 5a). However, on the inner forereef rugosity rapidly decreases with distance

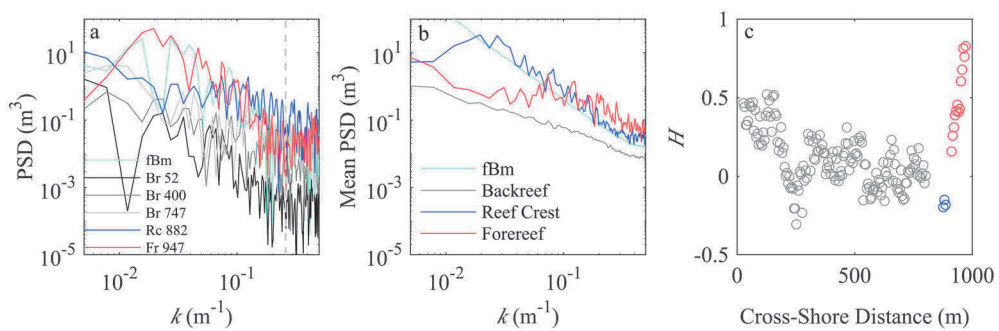


**Figure 6.** (a) Power spectra, for example, transects from the backreef (Br 52, Br 400, and Br 747), reef crest (Rc 882), and forereef (Fr 947), as well as an fBm signal ( $H = 0.75$ ). Dashed line indicates location of scale break near  $0.26 \text{ m}^{-1}$ . (b) Mean power spectra for the three zones as well as 1,000 fBm transects defined by  $H = 0.75$ . (c) Hurst exponents (without multifractal correction), averaged over every five transects, computed from the slope of the power spectra,  $\beta$ , as a function of cross-shore distance.

### 3.3. Power Spectrum

The Hurst exponent,  $H$ , was computed from the slope of the power spectra in an identical manner for both idealized fBm series and reef bathymetric transects (Figure 6). Examples of power spectra for an fBm series ( $H = 0.75$ ) as well as transects from the three reef zones are shown in Figure 6a. Although the decay in spectral density is approximately linear across most of the wave number range for the reef transects, significant scale breaks do occur near the high-wave number end of the spectrum, such as the break in the fr 947 spectrum around  $0.26 \text{ m}^{-1}$ . As Gagnon et al. (2006) show, breaks can occur for individual transects (realizations) that have been extracted from a process with perfect scale invariance, due to statistical variability. Therefore, to estimate the scaling for an entire reef zone, it is important to ensemble average power spectra of many transects (Figure 6b; Gagnon et al., 2006). Average  $H$  estimated from the slope of the spectral density across the scale range  $4 \leq 1/k \leq 256$  is 0.73 for 1,000 fBm transects (close to the theoretical value of  $H = 0.75$  that defines the covariance structure).

Although there is some scatter in  $H$  between adjacent transects due to statistical variability in the power spectra, there is evidence of cross-shore trends in global scaling (Figure 6c). There is a wide distribution of  $H$  values across the three zones. The exponent  $H$  decreases with increasing distance from shore in the backreef is relatively low on the reef crest and increases linearly with distance from shore on the forereef. The highest values of  $H$  are associated with forereef topography and the lowest  $H$  values are associated with reef crest topography. For some backreef and reef crest transects, the value of  $H$  is negative. Negative values of  $H$  signify larger fluctuations at high wave numbers than at low wave numbers (Lovejoy & Schertzer, 2012). This is consistent with the size of the fluctuations observed in spatial series. Overall, the mean Hurst exponents (computed without the multifractal correction) are 0.06,  $-0.12$ , and 0.51 for the backreef, reef crest, and forereef transects (Figure 6c).

### 3.4. Multifractal Spectrum

We can determine a statistical distribution of local scaling exponents ( $h$ ) from the wavelet leaders,  $l_x(s, x)Z(s, q)$  and  $s$  was approximately linear for all values of  $q$ . Figure 7e shows the variance versus spatial scale and is analogous to the power spectrum. For monofractal processes, such as fBm, the change in the slope of the regression between  $Z(s, q)$  and  $s$  (i.e.,  $\tau(q)$ ) as a function of  $q$  is approximately linear (Figure 8a). Therefore,  $h = d\tau(q)/dq$  is constant and the multifractal spectrum,  $D(h)$  (equation (12)), which is analogous to a probability distribution of Hölder exponents, clusters around the point  $(H, D(H))$ . For the fBm series (see Figure 8b),  $D(h)$  clusters around the point  $(0.75, 1)$ . For monofractal processes the theoretical spectra have no width or asymmetry ( $c_2 = 0$  and  $c_3 = 0$ ).

For the reef bathymetry,  $\tau(q)$  changes nonlinearly as a function of  $q$  (Figure 8a), indicating that the bathymetry is multifractal. This means that the scaling of the topography varies across the spatial signal so that

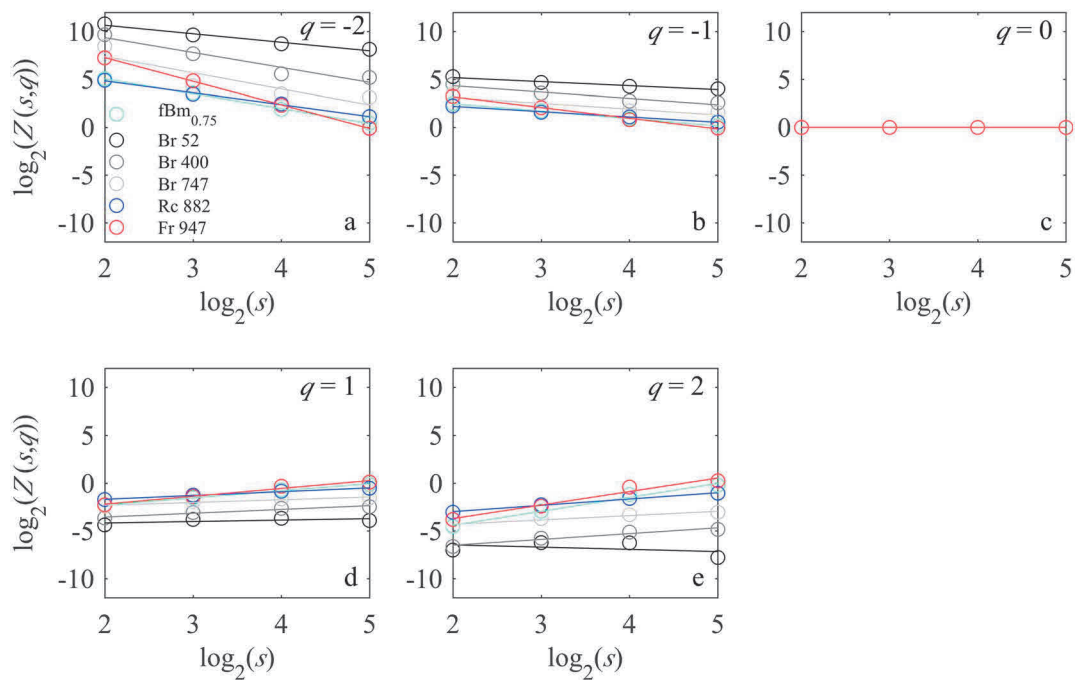


**Figure 7.** (a–e) Linear fits to the partition function,  $Z(s, q)$ , for selected values of  $q$  for the same example transects shown in Figure 5.

a distribution of Hölder exponents ( $h$ ) is needed to characterize the local scaling behaviors. In addition to the statistically dominant  $h(c_1)$ , which corresponds to the location of the maximum of  $D(h)$ , the width ( $c_2$ ) and the asymmetry ( $c_3$ ) of the multifractal spectrum provide additional information about local scaling behaviors not captured by monofractal techniques. For example, while different backreef transects (Br 51, Br 400, and Br 747) exhibit similar dominant scaling behavior ( $c_1 = 0.35, 0.52$ , and  $0.40$ , respectively), Br 51 and Br 747 have opposite asymmetry ( $c_3 = -0.38$  and  $0.33$ , respectively; Figure 8b). For transect Br 51, the negative asymmetry indicates local scaling exponents greater than the spectral peak ( $c_1 = 0.35$ ) are more prevalent in the spatial series than scaling exponents less than  $c_1 = 0.35$ , as indicated by greater  $D(h)$  values at these points. For transect Br 400, the spectrum is approximately symmetric ( $c_3 = 0.03$ ). The three transects also display variable widths, as Br 51 is the narrowest ( $c_2 = -0.23$ ), followed by Br 400 ( $c_2 = -0.28$ ) and Br 747

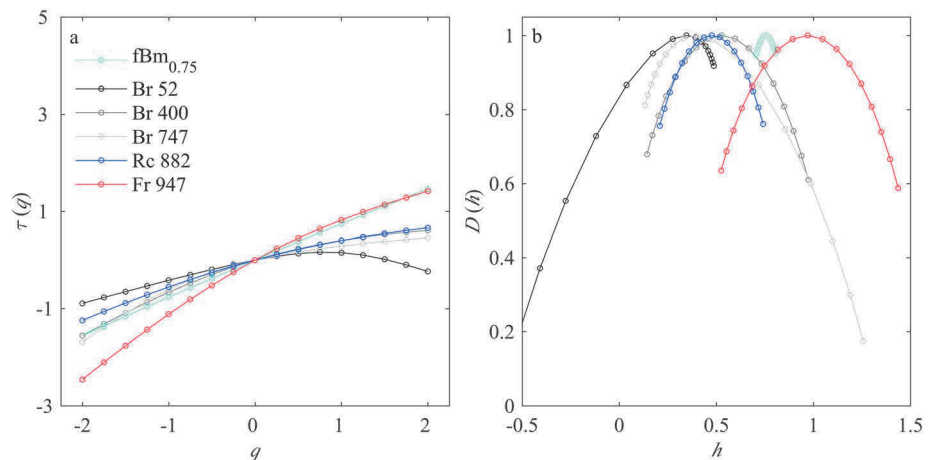


**Figure 8.** Estimates of (a)  $\tau(q)$  and (b)  $D(h)$  for the example transects shown in Figures 5 and 6 computed using the wavelet leaders method.

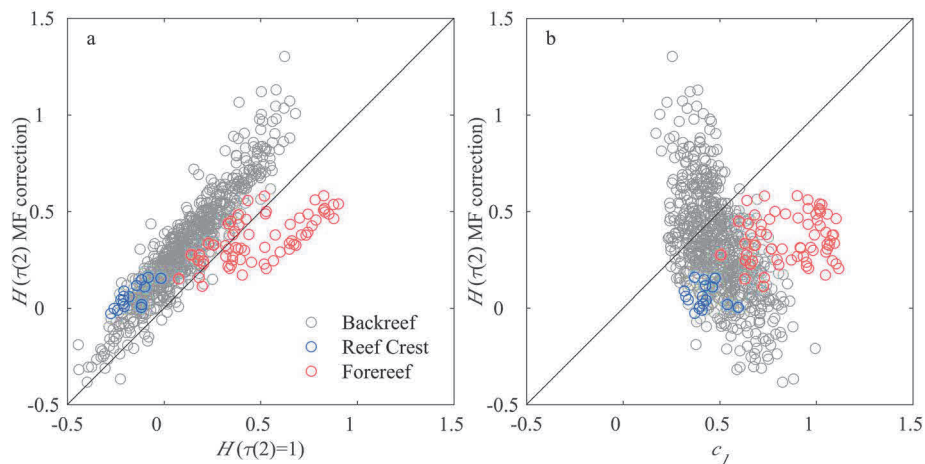


**Figure 9.** (a) Hurst exponent,  $H$ , with and without second-order multifractal correction,  $\tau(2)$ , for each transect in the three reef zones. (b) Relationship between the statistically dominant local Hölder exponent,  $c_1$ , and the global Hurst exponent. Black solid lines indicate perfect agreement between the two values in (a) and (b), as would be expected for monofractal signals defined everywhere by a single scaling exponent, such as fBm.

( $c_2 = -0.30$ ). A wider spectrum indicates that a series possesses a wider range of Hölder exponents. Note that by definition,  $c_2$  is negative because  $D(h)$  is concave.

Generally, the lowest dominant Hölder exponent ( $c_1$ ) values ( $c_1 < 0.5$ ) correspond to sections of the backreef ( $x < 0.25$  km and  $x < 0.65$  km) and reef crest (Figure 5e). In the backreef, 55% of all transects had  $c_1$  values less than 0.5 compared to 88% on the reef crest. This implies highly irregular, anticorrelated topography that is consistent with our qualitative knowledge of the irregular coral topography in these zones. The middle section of the backreef ( $0.25 < x < 0.65$  km) coincides with an area of lower bottom elevation and lower standard deviation (Figures 2 and 5a), and 76% of transects in this section had values in the range  $0.4 < c_1 < 0.7$ , indicating slightly more autocorrelated topography. On the forereef,  $c_1$  linearly increases with cross-shore distance and has values in the range  $0.6 < c_1 < 1$ . In this zone, 97% of the transects had  $c_1$  values greater than 0.6, suggesting highly autocorrelated topography over long distances, which is consistent with the spur and groove structures found in this zone.

Spectral width ( $c_2$ ) is weakly negatively correlated with  $c_1$  ( $r = -0.48$ ), such that bathymetric transects with low  $c_1$  values have narrower spectra and transects with high  $c_1$  values have wider spectra (Figures 5e and 5f), indicating greater multifractality and a wider range of scaling behaviors in the topography. The sign of the spectral asymmetry parameter ( $c_3$ ) changes from negative for the backreef section closest to shore to positive for the backreef section furthest from shore (Figure 5g). This suggests that for backreef transects closer to shore, Hölder exponents greater than the value at the peak of the multifractal spectrum are more prevalent than Hölder exponents less than the value at the peak. For backreef transects with similar  $c_1$  values, this suggests that transects close to shore have more autocorrelated topography than transects further from shore despite the statistically dominant Hölder exponent being the same. Furthermore, spectral asymmetry changes from weakly positive on the reef crest to weakly negative on the outer forereef. These less dominant scaling behaviors further suggest that the topography on the outer forereef is more autocorrelated than the topography on the reef crest and inner forereef.

One would expect that the scaling exponents computed using spectral density and wavelet leaders methods would not agree given evidence that the bathymetry is multifractal, and therefore, global and local scaling behaviors may differ (Lovejoy & Schertzer, 2007). This means that the assumption  $\tau(2) = 1$  is valid for quasi-Gaussian fBm but not for natural topography, as demonstrated by Gagnon et al. (2006).  $H$  values computed with the multifractal correction were higher than those without the correction on the backreef and reef crest and lower than without the correction for much of the forereef (Figure 9a). We also compared the statistically dominant local scaling exponent from the wavelet leader method ( $c_1$ ) to  $H$  computed using the spectral density method with the multifractal correction (Figure 9b);  $c_1$  was consistently greater than  $H$

for reef crest and fore reef transects. For the backreef, there was a very large range of  $H$  among transects but a much smaller range of  $c_1$ , and  $H$  values varied from much larger than to much smaller than  $c_1$  for the same transects (Figure 9b).

## 4. Discussion

### 4.1. Roughness Metrics

#### 4.1.1. Moments of the Distribution

The first four moments of the distribution of bottom elevation capture unordered spatial information at a single horizontal resolution contained in bathymetric series. These metrics provide a limited description of bathymetric complexity because they do not preserve the spatial arrangement of the data points. However, the moments of the distribution do describe the bathymetry in terms that have a physical interpretation, and as such can be directly related to some ecological (e.g., body size) and hydrodynamic (e.g., wave excursion amplitude) parameters. For example, in the past the physical height of bathymetric features has been inferred from the standard deviation and used to represent hydrodynamic roughness lengths along the reef (Lowe et al., 2005). The straightforward computation of these metrics permits reliable comparison between bathymetry at different sites or over time, as long as the horizontal resolution of the measurements is preserved. Both standard deviation, which increases with distance from shore as the amplitude of bathymetric features (e.g., channels, spur, and groove) increases, and skewness, which decreases with distance from shore as the amplitude of channels and grooves increases relative to the amplitude of coral bommies and spurs, can be used to differentiate the three reef zones because they are significantly different at the 95% confidence level ( $p < 0.05$ ). While the standard deviation is positively correlated with  $H$  for the fBm series (Figure 3), fBm has a Gaussian distribution with zero skewness and therefore is limited as a model for natural reef bathymetry.

#### 4.1.2. Rugosity

The greatest range in rugosity values was associated with fore reef topography, which included the entire range of values found on the reef crest and part of the backreef. This implies that rugosity alone cannot differentiate between fore reef topography (dominated by low-wave number spur and groove features) and reef crest topography (characterized by coral rubble intersected by narrow channels). The rms slope  $(db/dx)_{rms}$  for the same transects exhibited very similar spatial patterns due to the similar functional form (cf. equations (5) and (6)) and high correlation with rugosity.

#### 4.1.3. Hurst and Hölder Exponents

Global and local scaling behaviors, which represent the change in bathymetric variability across a range of spatial scales, were quantified using Hurst,  $H$ , and Hölder,  $h$ , exponents. While the values of  $H$  and dominant Hölder exponent ( $c_1$ ) were generally not equal for a given bathymetric transect, cross-shore trends in these two quantities were consistent. For example, on the fore reef  $H$  and  $c_1$  both linearly increase with distance from shore because most of the transects intersect the same spur and groove features, which become wider and more regular further offshore. On the reef crest,  $H$  and  $h$  also increase with distance from shore due to small, narrow channels incising adjacent transects. In the backreef, weaker spatial autocorrelation of the scaling behaviors in the cross-shore direction is due to the presence of randomly distributed coral bommies less than or similar in size to the horizontal resolution of the data. While cross-shore trends may be similar, the values of  $H$  and  $h$  depend on the choice of method as well as associated user-defined parameters (e.g., window or wavelet choice).

Our results reveal the multifractal behavior of coral reef bathymetry, evident by the nonlinear relationship between  $\tau(q)$  and  $q$ , which is consistent with nonhomogeneous functions with multifractal properties (Arneodo et al., 2002). For these functions,  $h$  is a fluctuating quantity that varies with position along the spatial series (Arneodo et al., 2002). We found that the spectral peak and the spectral width and asymmetry vary widely across a relatively short spatial extent of the reef ( $\sim 1$  km). This was expected given the heterogeneity of physical structures present across the three reef zones but represents a departure from some terrestrial topographic studies that have identified a narrow, characteristic range of scaling behaviors (Weissel et al., 1994). In general,  $c_1$  was less than 0.5 on the backreef and reef crest indicating rough, anticorrelated topography and greater than 0.5 on the fore reef, indicating smooth, correlated topography (Figure 5e). The width ( $c_2$ ) and asymmetry ( $c_3$ ) of the multifractal spectrum provide additional information about the existence and prevalence of other scaling behaviors in the bathymetry. The high autocorrelation in  $c_1$ ,  $c_2$ , and  $c_3$  in

the cross-shore direction suggests that adjacent transects have similar spectral properties (Figures 5f and 5g). The multifractality of the natural reef bathymetry calls into question the suitability of fBm as a model for reefs and highlights the need to evaluate multifractal models for reef bathymetry.

A major limitation of using the scaling behavior to characterize bathymetric roughness is that it does not provide information about the physical size of bathymetric features. This could potentially be estimated using the  $y$  intercept of the power law relationship (Weissel et al., 1994). However, the value of the  $y$  intercept depends on the choice of monofractal method (e.g., power spectral density (PSD)). Additionally, for the wavelet leaders technique, the  $y$  intercept of  $Z(s, 0)$  does not represent the amplitude of bottom elevation variations but rather the number of leaders at the smallest scale.

#### 4.2. Multifractality of Natural Topography

In this study, coral reef topography was found to be multifractal. Multifractals are commonly found in geophysical studies, particularly across natural textures and topography formed by nonlinear processes operating across a wide range of spatial scales (Gangodagamage et al., 2007; Lashermes & Foufoula-Georgiou, 2007; Lavallée et al., 1993; Niedermeier et al., 2000; Ródenas & Garello, 1998). For example, studies have demonstrated the multifractality of forest canopies using both the wavelet leaders (Wendt et al., 2009) and other (Drake & Weishampel, 2000; Widłowski et al., 2001) techniques. The evidence of multifractal scaling in both forest and coral canopies is important because forest canopies offer potentially useful terrestrial analogs for understanding boundary layer flow over certain reef morphologies.

Multifractality has also been demonstrated using the wavelet leaders technique in mountain ranges where heterogeneous tectonic processes form complex topography characterized by a range of scaling exponents over a narrow spatial extent (Kolahi-Azar & Golriz, 2018). Our results similarly show heterogeneous scaling for one-dimensional transects extracted from a relatively narrow bathymetric swath in part due to different hydrodynamic processes operating on the backreef (Hench & Rosman, 2013), reef crest (Hench et al., 2008), and forereef (Monismith et al., 2013; Rogers et al., 2013).

Other studies have found that the change in topographic variation with spatial scale may vary depending on the scale range considered. Topography may be well characterized by a single global exponent (monofractal) at small scales but may be best described by many local exponents at larger scales (multifractal; Deliège et al., 2016, 2017) due to different geophysical processes operating at different spatial scales. Our results did not show the presence of both monofractal and multifractal scaling regimes, possibly due to the limited spatial resolution and extent of our data, which spanned 2 orders of magnitude.

We caution against cross-study comparisons of scaling exponents for different topographic data sets even if the same multifractal technique is utilized due to differences in horizontal spatial resolution, scale range over which exponents are computed, data dimensionality (one-dimensional spatial series vs. two-dimensional spatial field), as well as averaging and subsampling techniques used during data processing that affect the autocorrelation of the spatial series or field (Lavallée et al., 1993).

#### 4.3. Collapsing Complexity

The number and type of metrics used to characterize roughness determine the degree to which bathymetric complexity is collapsed and which topographic properties are represented. The most appropriate set of metrics to describe multiscale topographic variation will depend on the application. For our reef data set, descriptors of the elevation distribution such as the standard deviation and skewness are sufficient to differentiate between the three reef zones (Figure 5). However, considering metrics that describe how topography varies with spatial scale (e.g., Hölder exponent), together with properties of the elevation distribution and ratios of physical length scales, provides a more complete understanding of how the topography varies between and within reef zones.

A principal component analysis (PCA) was performed to investigate the degree to which different metrics covary across the reef and to identify the combination of metrics that best distinguished dissimilar bathymetry among and within reef zones. The metrics included in the PCA were the standard deviation ( $\sigma$ ) and skewness ( $S$ ) of the bottom elevation, rugosity ( $R$ ), and the dominant Hölder exponent value ( $c_1$ ) and the width ( $c_2$ ) of the multifractal spectrum.

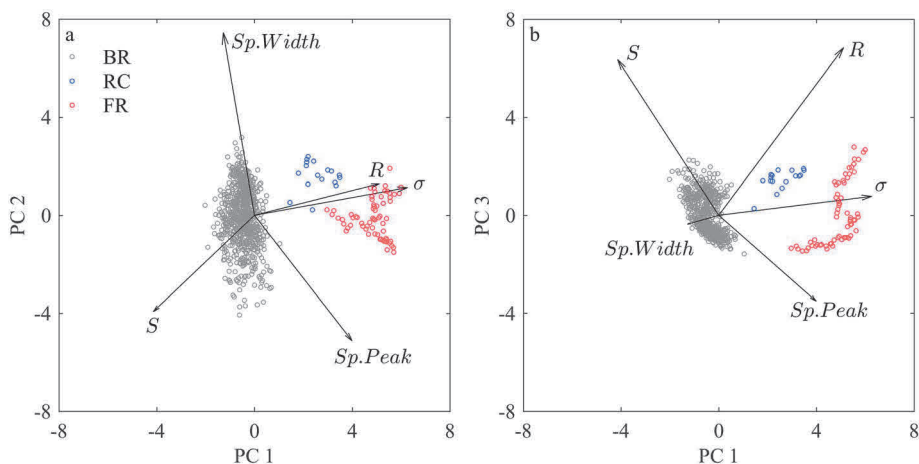


**Figure 10.** Principal component (PC) 1, 2, and 3 scores for backreef (gray), reef crest (blue), and forereef (red) transects. Vectors show the orthonormal PC coefficients multiplied by a factor of 10 for each variable indicating the contribution of a given variable to the PCs.

The first, second, and third principal components explain 89.8% of the total variability in these metrics among alongshore transects (47.2%, 28.2%, and 14.4%, respectively; Figure 10). The first principal component (PC1) describes the primary mode of topographic variability in the data set and captures the way the metric values vary among the three main reef zones. The standard deviation (loading  $L = 0.63$ ), rugosity ( $L = 0.51$ ), and dominant Hölder exponent ( $L = 0.40$ ) are positively correlated along PC1, and skewness ( $L = -0.41$ ) is negatively correlated (Figure 10). PC1 scores are negative for the backreef, weakly positive for the reef crest, and strongly positive on the forereef. Negative scores for backreef transects correspond to topography with low standard deviation and rugosity, and Hölder exponents less than 0.5, indicating low-amplitude, spatially incoherent topography (see also Figure 5). Positive scores for forereef transects correspond to topography with high standard deviation and rugosity, and Hölder exponents greater than 0.5, indicating high-amplitude, autocorrelated topography (Figures 5 and 10).

Along PC2, the spectral width ( $L = 0.74$ ) varies negatively with the Hölder exponent ( $L = -0.51$ ) and skewness ( $L = -0.39$ ). PC2 generally captures the way these parameters covary across the backreef. Along PC3, the rugosity ( $L = 0.68$ ) and skewness ( $L = 0.63$ ) are positively correlated, and the Hölder exponent ( $L = -0.35$ ) is negatively correlated. The contribution of standard deviation to PC3 is very small ( $L = 0.08$ ). PC3 therefore represents topographic variability in which rugosity varies but standard deviation does not, such as on the inner forereef where small-scale features reduce in amplitude with distance from shore but large-scale large amplitude spur and groove features remain.

Although five metrics were used in the PCA, the first three principal components captured the main patterns in metrics within and among the reef zones. PC1 is sufficient to distinguish between the backreef, reef crest, and forereef topography. For this reef, PC1 explains much of the variance in rugosity and standard deviation across the three zones, and these two metrics are positively correlated. PC2 and PC3 provide additional information about within-zone variability. PC3 explains much of the variability in rugosity across transects within a particular zone that is not associated with variation in standard deviation. Examples drawn from both natural and idealized topographies illustrate that while topography with higher-amplitude features is generally more rugose, standard deviation and rugosity are not necessarily correlated if the horizontal length scale (e.g., wavelength in Figure 1) or scaling behavior changes.

#### 4.4. Implications for Reef Processes

Many studies have investigated relationships between the structural complexity of the seafloor and reef processes. In these studies, seafloor complexity is most often quantified using rugosity (Graham & Nash, 2013). Since rugosity represents a ratio of surface area to plan area, it may be an appropriate metric to use for questions in which the key seafloor property is surface area, such as fluxes of gases and nutrients (Falter et al., 2005; Thomas & Atkinson, 1997). However, our work illustrates that rugosity alone is not suitable as a

general measure of seafloor roughness or complexity, because the same rugosity value can be obtained for very different topographies, if horizontal length scales vary or multiple length scales are present (Figures 1 and 5). Some previous studies have noted inconsistent correlations between roughness, quantified by rugosity, and the abundance, size distribution, and diversity of reef biota (e.g., Harborne et al., 2012). Further work is needed to determine whether relationships between patterns in reef biota and topographic properties could be more clearly seen using multiple metrics of topographic complexity that capture both the amplitude of topographic variations and the way in which vertical variations change with horizontal spatial scale. Increased resilience and recovery of reefs from disturbances have also been positively correlated with topographic complexity (e.g., Guzman & Cortés, 2007). Therefore, to better manage and predict future reef states, it is important to understand and quantify the attributes of reef structure that contribute to these reef state changes.

Another application for which characterizing topographic roughness is important is parameterizing the effect of the seafloor on water motion. Drag exerted on the flow by topography is typically represented using a roughness length scale (e.g.,  $k_b$  and  $z_0$ ). In previous work on coral reefs, hydrodynamic roughness has been related to the standard deviation of topographic elevation (Lowe et al., 2005) and the rms bottom slope (Rogers et al., 2018). Prior studies on atmospheric boundary layers have shown that for topography with a constant scaling,  $z_0$  is proportional to the standard deviation of topographic elevation (Wan & Porte-Agel, 2011). However, the constant of proportionality varies over several orders of magnitude depending on the power law scaling behavior (Anderson & Meneveau, 2011), which is related to the Hurst exponent. This previous work suggests that if topography can be described with a single power law scaling exponent, then the effects of the topography on flow can be represented with just the standard deviation and scaling exponent. Other work, however, has found that heterogeneity (patchiness) of surface roughness properties can increase drag and results in an effective roughness length scale that is larger than the roughness length scale characterizing any given patch of topography (Albertson & Parlange, 1999; Bou-Zeid et al., 2004, 2007). The more frequently surface properties change, the larger the effective roughness felt by the flow. This suggests the need for multifractal metrics such as those that can be obtained from the multifractal spectrum (spectral peak, width, and asymmetry) that capture not only the total variance and average scaling of topography but also the spatial variability of those properties. For this study, the spatial scale range included in the multifractal analysis is large compared to the depth of the water and thus better describes the bathymetry rather than roughness felt by the flow. Additional analysis of multifractal properties at submeter scales is needed to characterize the hydrodynamically relevant roughness.

## 5. Conclusion

Because seafloor topography affects a wide range of physical and biological processes, collapsing the complex three-dimensional structure of the bottom to statistical metrics that quantify its important properties is a common challenge in studies of marine systems. Here we investigated this issue by calculating a variety of metrics for idealized single-scale and multiscale topographies and real reef topography. We illustrated that the most commonly used metrics, standard deviation and rugosity, are not sufficient to quantify bottom roughness and give ambiguous results when horizontal length scales vary or when multiple length scales are present. For multiscale topography, it is important to also quantify scaling behavior, the rate at which the variance in the bottom elevation decays with decreasing spatial scale.

We computed a global Hurst exponent from the spectral density, as well as the distribution of local Hölder exponents from the wavelet leader method to characterize the scaling behavior of both idealized monofractal and real multifractal reef topography. For the real reef topography, cross-shore trends in Hurst and Hölder exponents derived from monofractal and multifractal methods were consistent, but the actual values differed, as is often the case for multifractal signals. A distribution of Hölder exponents was needed to describe the scaling behavior of the multifractal reef topography.

Our results demonstrate that coral reef topography, similar to other natural topography, is both multiscale and multifractal. While quantifying roughness with a single metric that captures a moment of the elevation distribution, dimensionless ratio of physical length scales, or how elevation varies with spatial scale may suffice for some applications, it is useful to consider metrics from all three categories (e.g., standard deviation, rugosity, and dominant Hölder exponent). A PCA allowed us to collapse the complete set of metrics to a

smaller number of dominant modes and investigate the degree to which the metrics covaried or varied independently across the three zones on the Moorea reef. Collectively, the results show that individual metrics can capture specific attributes of topography, but a greater proportion of topographic variability is explained by considering different types of metrics together as a set.

## Acknowledgments

Support for this work came from the National Science Foundation Physical Oceanography program (OCE-1435530 and OCE-1435133). Airborne lidar bathymetry data collection was supported by the NSF LTER program (OCE-1637396). M. Duvall gratefully acknowledges support from a Duke University Dean's Fellowship. We thank G. Katul for thoughtful discussions about representing roughness and D. Holstein for insights into principal components. We thank three anonymous reviewers for their thoughtful comments that improved the manuscript. This research was conducted under permits issued by the French Polynesian Government (Délégation à la Recherche) and the Haut-commissariat de la République en Polynésie Française. Data in this work are archived and available in the NSF LTER data repository (<https://doi.org/10.6073/pasta/ae823cf0473bbc29461a19a13418b557>).

## References

- Abry, P., & Sellan, F. (1996). The wavelet-based synthesis for fractional Brownian motion proposed by F. Sellan and Y. Meyer: Remarks and fast implementation. *Applied and Computational Harmonic Analysis*, 3(4), 377–383. <https://doi.org/10.1006/acha.1996.0030>
- Albertson, J. D., & Parlange, M. B. (1999). Surface length scales and shear stress: Implications for land-atmosphere interaction over complex terrain. *Water Resources Research*, 35(7), 2121–2132. <https://doi.org/10.1029/1999WR900094>
- Anderson, W., & Meneveau, C. (2011). Dynamic roughness model for large-eddy simulation of turbulent flow over multiscale, fractal-like rough surfaces. *Journal of Fluid Mechanics*, 679, 288–314. <https://doi.org/10.1017/jfm.2011.137>
- Arneodo, A., Audit, B., Decoster, N., Muzy, J. F., & Vaillant, C. (2002). Wavelet based multifractal formalism: Applications to DNA sequences, satellite images of the cloud structure and stock market data. In A. Bunde, J. Kropp, & H. J. Schellnhuber (Eds.), *The science of disasters: Climate disruptions, heart attacks, and market crashes* (pp. 26–102). Berlin, Germany: Springer. [https://doi.org/10.1007/978-3-642-56257-0\\_2](https://doi.org/10.1007/978-3-642-56257-0_2)
- Asher, S., Niewerth, S., Koll, K., & Shavit, U. (2016). Vertical variations of coral reef drag forces. *Journal of Geophysical Research: Oceans*, 121, 3549–3563. <https://doi.org/10.1002/2015JC011428>
- Atkinson, M. J., & Bilger, R. W. (1992). Effect of water velocity on phosphate uptake in coral reef-flat communities. *Limnology and Oceanography*, 37(2), 273–279. <https://doi.org/10.4319/lo.1992.37.2.0273>
- Bou-Zeid, E., Meneveau, C., & Parlange, M. B. (2004). Large-eddy simulation of neutral atmospheric boundary layer flow over heterogeneous surfaces: Blending height and effective surface roughness. *Water Resources Research*, 40, W02505. <https://doi.org/10.1029/2003WR002475>
- Bou-Zeid, E., Parlange, M. B., & Meneveau, C. (2007). On the parameterization of surface roughness at regional scales. *Journal of Atmospheric Science*, 64(1), 216–227. <https://doi.org/10.1175/JAS3826.1>
- Comeau, S., Edmunds, P. J., Lantz, C. A., & Carpenter, R. C. (2014). Water flow modulates the response of coral reef communities to ocean acidification. *Scientific Reports*, 4, 6681–6686.
- Dahl, A. L. (1973). Surface area in ecological analysis: Quantification of benthic coral-reef algae. *Marine Biology*, 23(4), 239–249. <https://doi.org/10.1007/BF00389331>
- Daubechies, I. (1990). The wavelet transform, time-frequency localization and signal analysis. *IEEE Transactions on Information Theory*, 36(5), 961–1005. <https://doi.org/10.1109/18.57199>
- Deliègle, A., Kleynssens, T., & Nicolay, S. (2016). Fractal nature of mars topography analyzed via the wavelet leaders method. In S. Latifi (Ed.), *Information Technology: New Generations: 13th international conference on information technology*, (pp. 1295–1298). Cham: Springer. [https://doi.org/10.1007/978-3-319-32467-8\\_117](https://doi.org/10.1007/978-3-319-32467-8_117)
- Deliègle, A., Kleynssens, T., & Nicolay, S. (2017). Mars topography investigated through the wavelet leaders method: A multidimensional study of its fractal structure. *Planetary and Space Science*, 136, 46–58. <https://doi.org/10.1016/j.pss.2016.12.008>
- Dennison, W. C., & Barnes, D. J. (1988). Effect of water motion on coral photosynthesis and calcification. *Journal of Experimental Marine Biology and Ecology*, 115(1), 67–77. [https://doi.org/10.1016/0022-0981\(88\)90190-6](https://doi.org/10.1016/0022-0981(88)90190-6)
- Drake, J. B., & Weishampel, J. F. (2000). Multifractal analysis of canopy height measures in a longleaf pine savanna. *Forest Ecology and Management*, 128(1–2), 121–127. [https://doi.org/10.1016/S0378-1127\(99\)00279-0](https://doi.org/10.1016/S0378-1127(99)00279-0)
- Falter, J. L., Atkinson, M. J., & Coimbra, C. F. M. (2005). Effects of surface roughness and oscillatory flow on the dissolution of plaster forms: Evidence for nutrient mass transfer to coral reef communities. *Limnology and Oceanography*, 50(1), 246–254. <https://doi.org/10.4319/lo.2005.50.1.0246>
- Falter, J. L., Atkinson, M. J., & Merrifield, M. A. (2004). Mass-transfer limitation of nutrient uptake by a wave-dominated reef flat community. *Limnology and Oceanography*, 49(5), 1820–1831. <https://doi.org/10.4319/lo.2004.49.5.1820>
- Friedlander, A. M., & Parrish, J. D. (1998). Habitat characteristics affecting fish assemblages on a Hawaiian coral reef. *Journal of Experimental Marine Biology and Ecology*, 224(1), 1–30. [https://doi.org/10.1016/S0022-0981\(97\)00164-0](https://doi.org/10.1016/S0022-0981(97)00164-0)
- Fugro LADS Corporation (2015). Airborne LIDAR bathymetric survey of French Polynesia 2015, Document number TLCS00.046.009, Prepared for J.L. Hench (PI), 188 pages.
- Gagnon, J. S., Lovejoy, S., & Schertzer, D. (2006). Multifractal earth topography. *Nonlinear Processes in Geophysics*, 13(5), 541–570. <https://doi.org/10.5194/npg-13-541-2006>
- Gangodagamage, C., Barnes, E., & Foufoula-Georgiou, E. (2007). Scaling in river corridor widths depicts organization in valley morphology. *Geomorphology*, 91(3–4), 198–215. <https://doi.org/10.1016/j.geomorph.2007.04.014>
- Goodchild, M. F. (1980). Fractals and the accuracy of geographical measures. *Mathematical Geology*, 12(2), 85–98. <https://doi.org/10.1007/BF01035241>
- Graham, N. A. J., & Nash, K. L. (2013). The importance of structural complexity in coral reef ecosystems. *Coral Reefs*, 32(2), 315–326. <https://doi.org/10.1007/s00338-012-0984-y>
- Guzman, H. M., & Cortés, J. (2007). Reef recovery 20 years after the 1982–1983 El Niño massive mortality. *Marine Biology*, 151(2), 401–411. <https://doi.org/10.1007/s00227-006-0495-x>
- Harborne, A. R., Mumby, P. J., & Ferrari, R. (2012). The effectiveness of different meso-scale rugosity metrics for predicting intra-habitat variation in coral-reef fish assemblages. *Environmental Biology of Fishes*, 94(2), 431–442. <https://doi.org/10.1007/s10641-011-9956-2>
- Hearn, C. J. (2011). Perspectives in coral reef hydrodynamics. *Coral Reefs*, 30(S1), 1–9. <https://doi.org/10.1007/s00338-011-0752-4>
- Hench, J. L., Leichter, J. J., & Monismith, S. G. (2008). Episodic circulation and exchange in a wave-driven coral reef and lagoon system. *Limnology and Oceanography*, 53(6), 2681–2694. <https://doi.org/10.4319/lo.2008.53.6.2681>
- Hench, J. L., & Rosman, J. H. (2013). Observations of spatial flow patterns at the coral colony scale on a shallow reef flat. *Journal of Geophysical Research: Oceans*, 118, 1142–1156. <https://doi.org/10.1002/jgrc.20105>
- Hurst, H. E. (1951). Long-term storage capacity of reservoirs. *Transactions of the American Society of Civil Engineers*, 116, 770–808.
- Jaffard, S., Lashermes, B., & Abry, P. (2006). Wavelet leaders in multifractal analysis. In T. Qian, M. I. Vai, & Y. Xu (Eds.), *Wavelet analysis and applications: Applied and numerical harmonic analysis* (pp. 219–264). Basel: Birkhäuser Verlag.

- Jaramillo, S., & Pawlak, G. (2011). AUV-based bed roughness mapping over a tropical reef. *Coral Reefs*, 30(S1), 11–23. <https://doi.org/10.1007/s00338-011-0731-9>
- Jones, N. L., Lowe, R. J., Pawlak, G., Fong, D. A., & Monismith, S. G. (2008). Plume dispersion on a fringing coral reef system. *Limnology and Oceanography*, 53(5, part2), 2273–2286. [https://doi.org/10.4319/lo.2008.53.5\\_part\\_2.2273](https://doi.org/10.4319/lo.2008.53.5_part_2.2273)
- Knudby, A., & LeDrew, E. (2007). Measuring structural complexity on coral reefs. Paper presented at 26<sup>th</sup> Proceedings of the American Academy of Underwater Sciences Symposium, Miami, USA.
- Kolahi-Azar, A. P., & Golriz, S. (2018). Multifractal topography: A tool to measure tectonic complexity in the Zagros Mountain Range. *Mathematical Geosciences*, 50(4), 431–445. <https://doi.org/10.1007/s11004-017-9720-z>
- Lashermes, B., & Foufoula-Georgiou, E. (2007). Area and width function of river networks: New results on multifractal properties. *Water Resources Research*, 43, W09405. <https://doi.org/10.1029/2006WR005329>
- Lashermes, B., Roux, S. G., Abry, P., & Jaffard, S. (2008). Comprehensive multifractal analysis of turbulent velocity using the wavelet leaders. *The European Physical Journal B*, 61(2), 201–215. <https://doi.org/10.1140/epjb/e2008-00058-4>
- Lavallée, D., Lovejoy, S., Schertzer, D., & Ladoy, P. (1993). Nonlinear variability and landscape topography: Analysis and simulation. In L. de Cola, & N. Lam (Eds.), *Fractals in Geography*, (pp. 171–205). Englewood, New Jersey: Prentice-Hall.
- Leichter, J. J., Alldredge, A. L., Bernardi, G., Brooks, A. J., Carlson, C. A., Carpenter, R. C., et al. (2013). Biological and physical interactions on a tropical island coral reef. *Oceanography*, 26(3), 52–63. <https://doi.org/10.5670/oceanog.2013.45>
- Lovejoy, S., & Schertzer, D. (1990). Our multifractal atmosphere: A unique laboratory for non-linear dynamics. *Physics in Canada*, 46(4), 62–71.
- Lovejoy, S., & Schertzer, D. (2007). Scaling and multifractal fields in the solid earth and topography. *Nonlinear Processes in Geophysics*, 14(4), 465–502. <https://doi.org/10.5194/npg-14-465-2007>
- Lovejoy, S., & Schertzer, D. (2012). Haar wavelets, fluctuations and structure functions: Convenient choices for geophysics. *Nonlinear Processes in Geophysics*, 19(5), 513–527. <https://doi.org/10.5194/npg-19-513-2012>
- Lovejoy, S., Schertzer, D., & Allaire, V. C. (2008). The remarkable wide range spatial scaling of TRMM precipitation. *Atmospheric Research*, 90(1), 10–32. <https://doi.org/10.1016/j.atmosres.2008.02.016>
- Lowe, R. J., Falter, J. L., Bandet, M. D., Pawlak, G., Atkinson, M. J., Monismith, S. G., & Koseff, J. R. (2005). Spectral wave dissipation over a barrier reef. *Journal of Geophysical Research*, 110, C04001. <https://doi.org/10.1029/2004JC002711>
- Luckhurst, B. E., & Luckhurst, K. (1978). Analysis of the influence of substrate variables on coral reef fish communities. *Marine Biology*, 49(4), 317–323. <https://doi.org/10.1007/BF00455026>
- Mallat, S. (2009). *A wavelet tour of signal processing: The sparse way*. Burlington, MA: Academic Press.
- Mandelbrot, B. B. (1975). Stochastic models for the Earth's relief, the shape and the fractal dimension of the coastlines, and the number-area rule for islands. *Proceedings of the National Academy of Sciences*, 72(10), 3825–3828. <https://doi.org/10.1073/pnas.72.10.3825>
- Mandelbrot, B. B., & van Ness, J. W. (1968). Fractional Brownian motions, fractional noises and applications. *SIAM Review*, 10(4), 422–437. <https://doi.org/10.1137/1010093>
- Martin-Garin, B., Lathuilière, B., Verrecchia, E. P., & Geister, J. (2007). Use the fractal dimensions to quantify coral shape. *Coral Reefs*, 26(3), 541–550. <https://doi.org/10.1007/s00338-007-0256-4>
- McCormick, M. I. (1994). Comparison of field methods for measuring surface topography and their associations with a tropical reef fish assemblage. *Marine Ecology Progress Series*, 112, 87–96. <https://doi.org/10.3354/meps112087>
- Meakin, P. (1998). *Fractals, scaling and growth far from equilibrium*. Cambridge, UK: Cambridge University Press.
- Monismith, S. G., Herdman, L. M. M., Ahmerkamp, S., & Hench, J. L. (2013). Wave transformation and wave-driven flow across a steep coral reef. *Journal of Physical Oceanography*, 43(7), 1356–1379. <https://doi.org/10.1175/JPO-D-12-0164.1>
- Muzy, J. F., Bacry, E., & Arneodo, A. (1993). Multifractal formalism for fractal signals: The structure-function approach versus the wavelet-transform modulus maxima method. *Physical Review E*, 47(2), 875–884. <https://doi.org/10.1103/PhysRevE.47.875>
- Muzy, J. F., Bacry, E., & Arneodo, A. (1994). The multifractal formalism revisited with wavelets. *International Journal of Bifurcation and Chaos*, 4(2), 245–302. <https://doi.org/10.1142/S021812749400204>
- Niedermeier, A., Romaneeben, E., & Lehner, S. (2000). Detection of coastlines in SAR images using wavelet methods. *IEEE Transactions on Geoscience & Remote Sensing*, 38(5), 2270–2281. <https://doi.org/10.1109/36.868884>
- Nunes, V., & Pawlak, G. (2008). Observations of bed roughness of a coral reef. *Journal of Coastal Research*, 24(2B), 39–50.
- Patterson, M. R., Sebens, K. P., & Olson, R. R. (1991). In situ measurements of flow effects on primary production and dark respiration in reef corals. *Limnology and Oceanography*, 36(5), 936–948. <https://doi.org/10.4319/lo.1991.36.5.0936>
- Purkis, S. J., & Kohler, K. E. (2008). The role of topography in promoting fractal patchiness in a carbonate shelf landscape. *Coral Reefs*, 27(4), 977–989. <https://doi.org/10.1007/s00338-008-0404-5>
- Purkis, S. J., Kohler, K. E., Riegl, B. M., & Rohmann, S. O. (2007). The statistics of natural shapes in modern coral reef landscapes. *Journal of Geology*, 115(5), 493–508. <https://doi.org/10.1086/519774>
- Purkis, S. J., Riegl, B. M., & Andréfouët, S. (2005). Remote sensing of geomorphology and facies patterns on a modern carbonate ramp (Arabian Gulf, Dubai, U.A.E.). *Journal of Sedimentary Research*, 75(5), 861–876. <https://doi.org/10.2110/jsr.2005.067>
- Risk, M. J. (1972). Fish diversity on a coral reef in the Virgin Islands. *Atoll Research Bulletin*, 193, 1–6.
- Ródenas, J. A., & Garello, R. (1998). Internal wave detection and location in SAR images using wavelet transform. *IEEE Transactions on Geoscience and Remote Sensing*, 36(5), 1494–1507. <https://doi.org/10.1109/36.718853>
- Rogers, J. S., Maticka, S. A., Chirayath, V., Woodson, C. B., Alonso, J. J., & Monismith, S. G. (2018). Connecting flow over complex terrain to hydrodynamic roughness on a coral reef. *Journal of Physical Oceanography*, 48(7), 1567–1587. <https://doi.org/10.1175/JPO-D-18-0013.1>
- Rogers, J. S., Monismith, S. G., Fedderson, F., & Storlazzi, C. D. (2013). Hydrodynamics of spur and groove formations on a coral reef. *Journal of Geophysical Research: Oceans*, 118, 3059–3073. <https://doi.org/10.1002/jgrc.20225>
- Sale, P. F., Douglas, W. A., & Doherty, P. J. (1984). Choice of microhabitats by coral-reef fishes at settlement. *Coral Reefs*, 3(2), 91–99. <https://doi.org/10.1007/BF00263759>
- Seuront, L. (2010). *Fractals and multifractals in ecology and aquatic science*. Boca Raton, FL: CRC Press.
- Tchiguirinskaia, I., Lu, S., Molz, F. J., Williams, T. M., & Lavallée, D. (2000). Multifractal versus monofractal analysis of wetland topography. *Stochastic Environmental Research and Risk Assessment*, 14(1), 8–32. <https://doi.org/10.1007/s004770050002>
- Thomas, F. I. M., & Atkinson, M. J. (1997). Ammonium uptake by coral reefs: Effects of water velocity and surface roughness on mass transfer. *Limnology and Oceanography*, 42(1), 81–88. <https://doi.org/10.4319/lo.1997.42.1.00081>
- Torre, C., & Compo, G. P. (1998). A practical guide to wavelet analysis. *Bulletin of the American Meteorological Society*, 79(1), 61–78. [https://doi.org/10.1175/1520-0477\(1998\)079<0061:APGTWA>2.0.CO;2](https://doi.org/10.1175/1520-0477(1998)079<0061:APGTWA>2.0.CO;2)

- Wan, F., & Porte-Agel, F. (2011). A large-eddy simulation study of turbulent flow over multiscale topography. *Boundary Layer Meteorology*, 141(2), 201–217. <https://doi.org/10.1007/s10546-011-9648-7>
- Watson, B. P., Lovejoy, S., Grosdidier, Y., & Schertzer, D. (2009). Scattering in thick multifractal clouds, Part I: Overview and single scattering. *Physica A*, 388(18), 3695–3710. <https://doi.org/10.1016/j.physa.2009.05.038>
- Weissel, J. K., Pratson, L. F., & Malinverno, A. (1994). The length-scaling properties of topography. *Journal of Geophysical Research*, 99(B7), 13,997–14,012. <https://doi.org/10.1029/94JB00130>
- Welch, P. D. (1967). The use of fast Fourier transform for the estimation of power spectra: A method based on time averaging over short, modified periodograms. *IEEE Transactions on Audio and Electroacoustics*, AU-15(2), 70–73.
- Wendt, H., Abry, P., & Jaffard, S. (2007). Bootstrap for empirical multifractal analysis. *IEEE Signal Processing Magazine*, 24(4), 38–48. <https://doi.org/10.1109/MSP.2007.4286563>
- Wendt, H., Roux, S. G., Jaffard, S., & Abry, P. (2009). Wavelet leaders and bootstrap for multifractal analysis of images. *Signal Processing*, 89(6), 1100–1114. <https://doi.org/10.1016/j.sigpro.2008.12.015>
- Widlowski, J., Pinty, B., Gobron, N., Verstraete, M. M., & Davis, A. B. (2001). Characterization of surface heterogeneity detected at the MISR/TERRA subpixel scale. *Geophysical Research Letters*, 28(24), 4639–4642. <https://doi.org/10.1029/2001GL013490>
- Wooding, R. A., Bradley, E. F., & Marshall, J. K. (1973). Drag due to regular arrays of roughness elements of varying geometry. *Boundary-Layer Meteorology*, 5(3), 285–308. <https://doi.org/10.1007/BF00155238>
- Yu, Z., Yee, L., & Zu-Guo, U. (2011). Relationships of exponents in multifractal detrended fluctuation analysis and conventional multifractal analysis. *Chinese Physics B*, 20(9). <https://doi.org/10.1088/1674-1056/20/9/090507>
- Zawada, D. G., & Brock, J. C. (2009). A multiscale analysis of coral reef topographic complexity using lidar-derived bathymetry. *Journal of Coastal Research*, 53, 6–15.
- Zawada, D. G., Piniak, G. A., & Hearn, C. J. (2010). Topographic complexity and roughness of a tropical benthic seascape. *Geophysical Research Letters*, 37, L14604. <https://doi.org/10.1029/2010GL043789>